

---

# REAL-TIME UAV COMPLEX MISSIONS LEVERAGING SELF-ADAPTIVE CONTROLLER WITH ELASTIC STRUCTURE

---

A PREPRINT

Mohamad Abdul Hady<sup>1</sup>, Basaran Bahadir Kocer<sup>2,3</sup>, Harikumar Kandath<sup>1</sup> and Mahardhika Pratama<sup>1</sup>.

<sup>1</sup>School of Computer Science and Engineering, Nanyang Technological University, 50 Nanyang Avenue, Singapore.  
*hady.elits@gmail.com*, *kharikumar@ntu.edu.sg*, *mpratama@ntu.edu.sg*

<sup>2</sup>School of Mechanical and Aerospace Engineering, Nanyang Technological University, 50 Nanyang Avenue, Singapore.  
*koce0001@e.ntu.edu.sg*

<sup>3</sup>Energy Research Institute @ NTU, Nanyang Technological University, 1 CleanTech Loop, Singapore.

January 11, 2022

## ABSTRACT

The expectation of unmanned air vehicles (UAVs) pushes the operation environment to narrow spaces, where the systems may fly very close to an object and perform an interaction. This phase brings the variation in UAV dynamics: thrust and drag coefficient of the propellers might change under different proximity. At the same time, UAVs may need to operate under external disturbances to follow time-based trajectories. Under these challenging conditions, a standard controller approach may not handle all missions with a fixed structure, where there may be a need to adjust its parameters for each different case. With these motivations, practical implementation and evaluation of an autonomous controller applied to a quadrotor UAV are proposed in this work. A self-adaptive controller based on a composite control scheme where a combination of sliding mode control (SMC) and evolving neuro-fuzzy control is used. The parameter vector of the neuro-fuzzy controller is updated adaptively based on the sliding surface of the SMC. The autonomous controller possesses a new elastic structure, where the number of fuzzy rules keeps growing or get pruned based on bias and variance balance. The interaction of the UAV is experimentally evaluated in real time considering the ground effect, ceiling effect and flight through a strong fan-generated wind while following time-based trajectories.

**Keywords:** Composite controller, evolving architecture, sliding mode controller, trajectory tracking, unmanned aerial vehicle interaction.

## 1 Introduction

The use of UAVs has already explored within the flying camera concept, where the system flies in the air in a passive manner [1]. Recently, the expectation of UAVs has shifted towards interaction operations in which the flying robot may interact and collaborate with cooperative or uncooperative objects, other robots and people in order to efficiently plan and execute the tasks. In most of these cases, UAV needs to conduct the flight in close proximities to objects, ground, ceiling or people [2],[3].

When the flying robots operate near objects, their aerodynamic properties might significantly change. For an autonomous aerial robot to anticipate these changes, it is required to include responsive, adaptive and resilient techniques. In this context, there is a need to inspire from nature where flying animals have attributes, including self-orientation and survival by predicting potential dangers. Since the aerodynamic properties of the rotors significantly change, the performance of the aerial robot may degrade in close proximity, which might result in a crash if the aforementioned properties are not included in the control system.

The ground effect observation is reported in landing problems, e.g. in [4],[5], and addressed in some implementations. This problem is considered in two stages in [6], descending phase and landing phase below 2 meters. The focus has been given to the localization aspects to obtain precise data when the system flies close to the ground. An outdoor

test is recorded in [7] with a 4 kg quadrotor system. In this implementation, the performance of the separate PID controllers for the attitude channel is presented but the altitude states are not discussed in terms of the ground effect. This approach is extended in [8],[9] for further experiments including lifting additional weights. A comprehensive study is presented in [10] by including an empirically fitted second order polynomial function in the model. This model is used from 40 cm above the ground in conjunction with the integral SMC. Its adaptive version without a ground effect model is experimentally investigated in [11]. Furthermore, a nonlinear controller based on backstepping is numerically investigated in [12]. This study is extended in [13],[14] by adding adaptive approach. In this context, an adaptive nonlinear disturbance observer is also added to the PID controller in [15] to compensate for the ground effect. In terms of real-time implementation, a nonlinear control approach based on a Lyapunov function is applied in [16] with a ground effect model. The input function is augmented for the vertical channel to suppress the disturbance due to the ground effect. Similarly, the PID controller is augmented in [17] with a robust compensator to mitigate the ground effect. An estimation-based approach is proposed in [18], where the ground effect is learned by the ant colony filter. In this numerical investigation, a sliding mode controller is implemented; however, the system needs to be adequately actuated to capture the ground effect efficiently. An additional estimation-based approach considering ring-source potential flow model is presented in [19]. Moreover, this problem is also investigated for fixed-wing UAVs during the landing considering the ground effect estimation for the controller [20].

The ground effect can degrade the system performance during landing and proximity flight to the ground. However, there is still a safety margin, where the ground effect creates an additional lift on the system. On the other hand, the ceiling effect pulls the flying object to the ceiling. Without a proper control strategy, this phenomenon can lead to a crash. In this context, the focus had given to generating an alternative path when the ceiling effect is detected in initial investigations [21],[22]. An exact opposite approach is explored in [23],[24], where the UAV is driven to be in contact with the ceiling. However, both approaches do not examine the case, where the system flies close to the ceiling by compensating the variable aerodynamic interactions. Since the thrust and drag coefficients of the propellers are changing during the flight in close proximity to ceiling, a variable control allocation matrix is proposed in [25]. This resulted in better performance. However, mapping and measuring these values are more troublesome in real-time experimental evaluations. A recent model-based approach is proposed in [26], where the model predictive controller (MPC) is utilized based on a nominal model of the system. The presented approach is promising but it requires a precise model and the optimization brings an additional computational cost [27].

A potential interaction can arise during the flight close to a vertical wall. However, this effect is milder as compared to the ground and ceiling effects. A more challenging task, e.g., flying in a UAV flock in tightly close formations, can be represented by flying through a fan along the horizontal axis. In this context, there are some alternatives already available in the literature to suppress the disturbance while tracking the commanded trajectories including MPC [28],[29], dynamic inversion control [30],[31], and adaptive control [32],[33]. Among them, SMC is one of the strong candidates to handle internal and/or external disturbances and the system uncertainties [34],[35]. In this context, SMC-based approaches are investigated in a simulated environment for the attitude and the position loops of the UAVs [36]. As a real-time experiment, a finite time stabilizing SMC is applied on a ground-based experimental setup [37]. However, the evaluation is restricted to the attitude channel of the system. Recently, a combination of PID and super twisting SMC are utilized to the UAV for the position control against disturbances [38]. Without loss of generality, the aforementioned nonlinear control approaches are associated with the accuracy of the plant dynamics and information about the operating environment. When the system goes into an interaction with the ceiling or the ground, the model of the UAV changes (e.g., variable thrust characteristics of the propeller). Similarly, flying through a fan might significantly affect the system. In this context, there are some learning-based approaches considered for UAV applications including fuzzy logic systems [39], neural networks [40],[41], and neuro-fuzzy-based control approaches [42],[43]. Furthermore, there are some approaches by combining different approaches, e.g., MPC with fuzzy logic control [44]. However, available learning-based approaches mostly using the fixed structured networks with fixed number of rules do not provide a flexible learning-scheme. Such controllers often lead to poor performance while performing complex flight missions without adequate retraining of the network or by using different combinations of the controller gains.

Recently, some evolving neuro-fuzzy controllers are proposed to tackle the varying system dynamics [45]. According to numerical investigations, it outperforms the PID (linear) and TS Fuzzy (nonlinear with fixed structure) controller. Nevertheless, it is evaluated within a simulation environment and it includes numerous parameter to be adjusted, which is arduous to be implemented in a real-time experiment with limited computational power. Another evolving controller was proposed based on neuro-fuzzy structure, which is a combination of an autonomous learning controller with the SMC [46]. This controller not only achieved better performance than the fixed structure ones, but also designed to be significantly less number of parameters by using hyperplane based membership function. Additionally, the proposed learning scheme is based on a three-layered neuro-fuzzy system with autonomous rule generation feature. By estimating bias and variance of the network, a structural evolution is aimed to achieve an optimum trade-off between under-fitting

and over-fitting condition. However, this work is evaluated only in a simulated environment for a simple mission like altitude control.

In this study, an autonomous controller with an elastic structure is proposed to solve the aforementioned problems inherent to UAV interaction and other challenging missions. Unlike in [46], where the input to the neuro-fuzzy structure contains the derivative of the error, here integral of error is used yielding better steady-state performance. In summary, the following novelties are presented in this study:

- For the first time, a composite controller comprising of SMC and an evolving neuro-fuzzy network structure is applied to an aerial robot performing complex missions.
- By estimating the network bias and variance, a new elastic structure based on neuro-fuzzy controller is implemented and evaluated for an aerial robot experimentally in real-time.
- The performance of the proposed controller is evaluated under ground and ceiling effect as well as circle and 8-shaped time-based trajectory tracking under wind disturbance.
- The proposed controller has been experimentally validated in the real-flight environments in which the flight videos can be found in <sup>1</sup>.
- The proposed method is generic and can be applied to any robotic missions without further tuning.

This paper is organized as follows: Section II formally describes the problem of trajectory tracking in the presence of external disturbances. Section III introduces the detailed structure, mechanism and update of the autonomous controller, namely Parsimonious Autonomous Controller (PAC). In Section IV, the experimental results and the corresponding analysis is discussed. Section V concludes the paper including the future work.

## 2 Problem Formulation

Based on the mission requirements, the UAV needs to navigate in challenging environments like in the proximity of a wall, ceiling or ground, or under external wind disturbances. In a region having obstacles, following a straight line trajectory connecting the current position and the desired position is not always feasible. Navigating in such regions require following of a circular or an 8-shaped trajectory [47]. Consider the first order dynamics of the UAV for trajectory control as given below

$$\dot{\eta}(t) = \dot{\eta}_o(t) + \dot{\eta}_d(t). \quad (1)$$

where  $\eta(t)$  is the position of the UAV,  $\dot{\eta}_o(t)$  is the UAV velocity (without disturbance) and  $\dot{\eta}_d(t)$  is the disturbance velocity input as shown in Fig. 1. Here the assumption is that the UAV is enabled with an inner loop velocity control to track the reference velocity input, ie.  $\dot{\eta}_o(t) \approx \dot{\eta}_r(t)$ . The unknown disturbance velocity input is due the effect of the wind disturbances and interaction effects. The controller  $\kappa(\cdot)$  is a mapping that relates the tracking error  $e_\eta(t)$  to the reference velocity input  $\dot{\eta}_r(t)$  as represented below

$$\dot{\eta}_r(t) = \kappa(e_\eta(t)). \quad (2)$$

The design of the controller poses some challenges as stated below.

- The reference trajectory  $\eta_r(t)$  is time-varying and having nonlinear time-dependent function. Moreover, the use of a controller with a fixed structure might not provide efficiency for tracking different reference trajectories under disturbances in an unknown environment [48].
- The power spectra of the wind disturbances is quite different from that of interaction effects. The controller should handle disturbances with unknown power spectra and those belonging to different categories.

The use of nonlinear robust control technique like SMC requires information about the upper bound of the disturbance acting on the system [49]. Using a conservative upper bound for different kinds of disturbances might result in the usage of large control effort. For tracking time varying trajectories in the presence of wind disturbances and interaction effects, an autonomous navigation algorithm with an evolving structure is proposed in this paper. The proposed trajectory tracking controller is composite consisting of a fixed sliding mode controller and a neuro-fuzzy system with varying number of fuzzy rules. The equations of motion for the trajectory tracking controller and the underlying assumptions are described below.

<sup>1</sup>Experimental video is available in: <https://youtu.be/-nGhMzvB7oE>

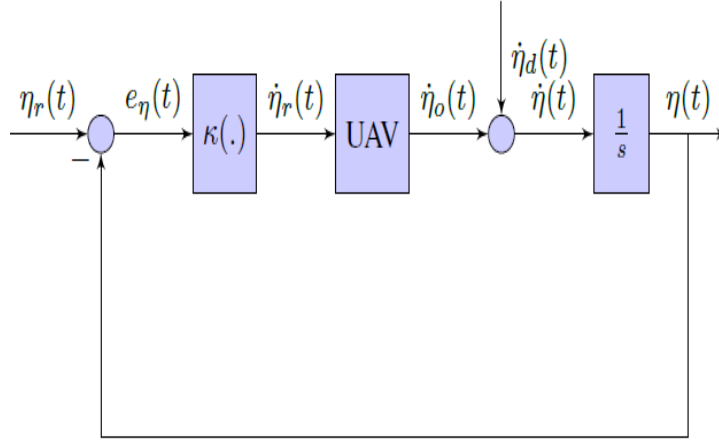


Figure 1: First order control architecture for the UAV with disturbances

The position of the UAV in the inertial frame is denoted by  $\eta(t)=(x, y, z)$ . The expanded version of (1) first order dynamics relating the reference velocity inputs  $\dot{\eta}_r(t)=(v_{xu}, v_{yu}, v_{zu})$ , disturbance velocity inputs  $\dot{\eta}_d(t)=(v_{xd}, v_{yd}, v_{zd})$  and the inertial position is given in (3), (4), and (5):

$$\dot{x} = v_{xu} + v_{xd}, \quad (3)$$

$$\dot{y} = v_{yu} + v_{yd}, \quad (4)$$

$$\dot{z} = v_{zu} + v_{zd}. \quad (5)$$

The objective is to develop an autonomous control algorithm to generate the reference velocity inputs  $(v_{xu}, v_{yu}, v_{zu})$ , to track the desired trajectory  $(x_r(t), y_r(t), z_r(t))$  in the presence of unknown disturbance velocity inputs denoted by  $(v_{xd}, v_{yd}, v_{zd})$ . The reference velocity inputs are tracked by the conventional inner loop PID controller, where a cascaded structure considering time scale differences between the translation and attitude dynamics is considered similar to [50]. The error vector and the error dynamics are given in (6) and (7),

$$\begin{bmatrix} e_x(t), e_y(t), e_z(t) \end{bmatrix}^T = \begin{bmatrix} x_r(t) - x(t), y_r(t) - y(t), z_r(t) - z(t) \end{bmatrix}^T, \quad (6)$$

$$\begin{pmatrix} \dot{e}_x(t) \\ \dot{e}_y(t) \\ \dot{e}_z(t) \end{pmatrix} = \begin{pmatrix} \dot{x}_r(t) - v_{xu} - v_{xd} \\ \dot{y}_r(t) - v_{yu} - v_{yd} \\ \dot{z}_r(t) - v_{zu} - v_{zd} \end{pmatrix}. \quad (7)$$

The following assumptions are utilized in this paper.

*Assumption I:* The reference trajectory  $(x_r(t), y_r(t), z_r(t))$  is uniformly continuous.

*Assumption II:* The disturbance velocity inputs  $(v_{xd}, v_{yd}, v_{zd})$  are bounded with unknown power spectra.

*Assumption I* and *Assumption II* enable the UAV to track the desired trajectory using bounded reference velocity inputs.

### 3 Parsimonious Autonomous Controller (PAC)

The structure of a quadrotor UAV control scheme using PAC is given in Fig. 2 for the case of  $x$  coordinate of the trajectory. Same architecture is used for the case of  $y$  and  $z$  coordinates and hence not discussed here separately. PAC is

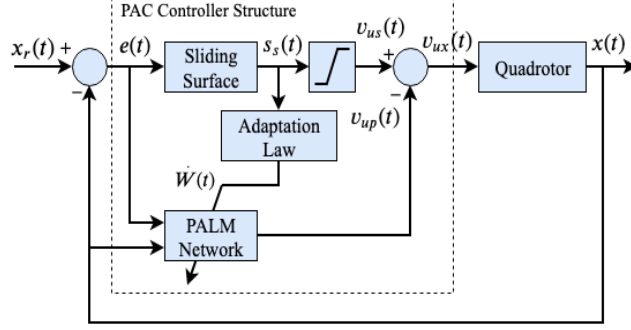


Figure 2: UAV control system block diagram for  $x$ -axis with PAC

constructed from SMC with a modification in the equivalent control input part to be adaptable. The sliding surface ( $s_s(t)$ ) posses the structure of a PID controller as given below

$$s_s(t) = k_1 e_x(t) + k_2 \int_0^t e_x(\tau) d\tau + k_3 \dot{e}_x(t). \quad (8)$$

where the gains  $k_1 > 0$ ,  $k_2 \geq 0$  and  $k_3 \geq 0$ . The velocity input from the sliding surface

$$v_{us} = \text{sat}(s_s(t)). \quad (9)$$

The saturation operation for any function  $f(t)$  with  $a_m > 0$  is defined as given below

$$\text{sat}(f(t)) = \begin{cases} f(t), & \text{if } (|f(t)| \leq a_m) \\ a_m \text{sign}(f(t)), & \text{if } (|f(t)| > a_m). \end{cases} \quad (10)$$

The adaptive part of the PAC is inherited from an autonomous learning machine namely PALM [51] to generate the input signal considering an unknown disturbance acting on the system. The architecture of PALM is given in Fig. 3. In this structure, the number of membership functions is equal to the number of rules denoted by  $r(t)$ . Unlike the conventional fixed structure of neuro-fuzzy, where the number of rules is pre-defined, here  $r(t)$  is the number of rules at a given time  $t$  and is time-varying due to its evolving feature. The neuro-fuzzy structure of PALM consists of three layers, namely: (i) input layer; (ii) fuzzification; (iii) inference and defuzzification. Each of these layers is discussed separately below.

(i) *Input layer*: The input is a combination of extended input (equal to 1), error, integral error, and the system output  $x(t)$ . The resulting input vector is given below

$$X_e = [1, e_x(t), \int_0^t e_x(\tau) d\tau, x(t)]^T. \quad (11)$$

(ii) *Fuzzification*: To transform the crisp value inputs into a fuzzy value, a hyperplane-based membership function  $\mu_i$  is selected in the fuzzification layer as given in (12) with  $i \in \{1, 2, 3, \dots, r(t)\}$

$$\mu_i = \exp\left(-\alpha \frac{\delta_i}{\max(\delta_i)}\right). \quad (12)$$

The parameter  $\alpha > 0$  and  $\delta_i$  is the normalized distance of the  $x_r$  from the  $i$ -th hyperplane ( $W_i X_e = 0$ ) as shown below

$$\delta_i = \left| \frac{x_r - (W_i X_e)}{\sqrt{W_i W_i^T}} \right|. \quad (13)$$

(iii) *Inference and Defuzzification*: Takagi-Sugeno fuzzy inference system is applied in this controller with each rule (Rule- $i$ ) statement as the following statement

$$\text{Rule-}i : \text{IF } X_e \text{ is Close to } \mu_i \text{ THEN } O_i = W_i \Lambda_i. \quad (14)$$

The output of each Rule- $i$  ( $O_i$ ) is obtained by multiplying the network parameter ( $W_i$ ) with  $\Lambda_i$  calculated from (15). It is observed that the proposed PAC controller incurs parsimonious network parameters compared to the conventional neuro-fuzzy controller in the literature because it is free of rule premise parameters. That is, the hyperplane functions are used in both rule premise and consequent part

$$\Lambda_i = \lambda_i X_e, \quad (15)$$

where the  $\lambda_i$  is the normalized firing strength of rule- $i$  calculated as:

$$\lambda_i = \frac{\mu_i}{\sum_{i=1}^R (\mu_i)}. \quad (16)$$

The final defuzzified (crisp) output is given by

$$v_{up} = \sum_{i=1}^R (O_i). \quad (17)$$

Furthermore, the reference velocity input to be given to the system ( $v_{ux}$ ) shown below is the difference of the output of SMC given in (9) and the defuzzified output given in (17)

$$v_{ux} = v_{us} - v_{up}. \quad (18)$$

The adaptation of PAC is implemented into two parts which is further discussed in the next two sub-sections. The first part is the adaptation of the elastic network structure (adjusting the number of rule ( $r(t)$ )) regulated by growing and pruning mechanism. The second part is the adaptation of network parameters ( $W_i(t)$ ) updated to minimize the cost function derived from the SMC output.

### 3.1 Elastic network structure adaptation mechanism

PAC starts its learning process from scratch with the absence of predefined network structure. Its structure is self-evolving with respect to the generalization power referring to the bias and variance trade-off in the machine learning literature. The expression of the mean squared error (MSE) for the network prediction is given below

$$MSE = \sum_{t^*=0}^T \frac{1}{T} (x[t^*] - x_p[t^*])^2, \quad (19)$$

where  $x[t^*]$  and  $x_p[t^*]$  is the sampled system output (UAV position along the x-axis) and the prediction output from the network respectively, within sampling interval  $0 < t^* \leq T$ . This equation raises further issues in the single-pass

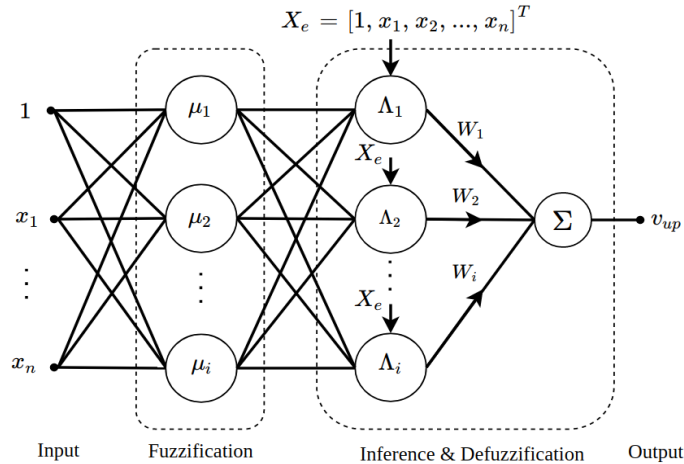


Figure 3: Neuro-fuzzy structure of PALM

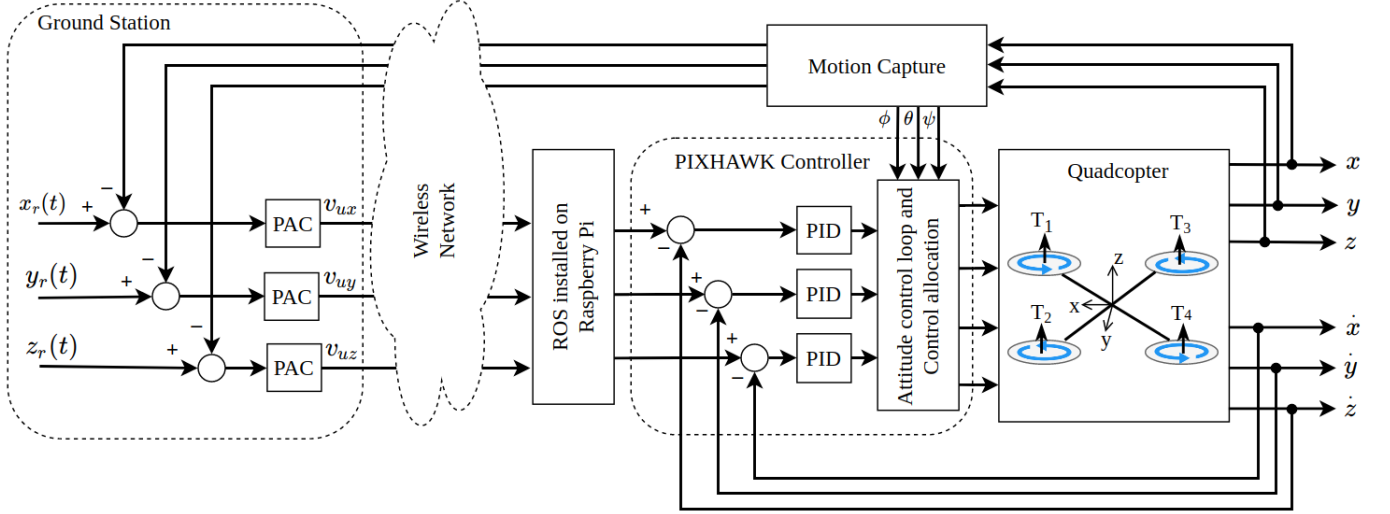


Figure 4: Architecture of the controller implementation

learning scenario due to: (i) the requirement of a memory to record all sampled data points to represent the network capacity, (ii) even though it can be calculated recursively without accumulating all of the sampled data, it can not represent the network capability for unseen input data samples, (iii) minimization of (19) leads to an unbiased estimator but risks on the overfitting situation. Thus, the network significance is re-formulated as given below

$$N_s = \int_{-\infty}^{\infty} (x - x_p(X_e))^2 f_p(X_e) dX_e, \quad (20)$$

where  $f_p(X_e)$  is the probability density function of the network input. The equation (20) is modified as shown below where  $E[\cdot]$  is the expectation operator

$$N_s = E[(x - x_p)^2]. \quad (21)$$

After implementing some algebraic operations, the following equation is obtained

$$N_s = (x - E[x_p])^2 + (E[x_p^2] - E[x_p]^2). \quad (22)$$

The first term of (22) denotes the bias ( $\beta_x^2$ ) and the second term corresponds to the variance ( $\vartheta_x$ ) of the network output as written below

$$N_s = \beta_x^2 + \vartheta_x. \quad (23)$$

To establish the bias and variance calculation in PAC, a unity rule firing strength ( $\lambda_i$ ) is assumed. It can simplify the network output as  $x_p = \sum_{i=1}^{r(t)} W_i X_e$ , because the expectation of the normalized firing strength does not have unique solution as the nature of hyperplane-based membership function. The expectation of  $x_p$  is re-written as given below

$$E[x_p] = \int_{-\infty}^{\infty} X_e W_i f_p(X_e) dX_e. \quad (24)$$

Assuming that the probability density function of  $X_e$  is normally distributed, the above equation is modified as given below

$$E[x_p] = W_i \mu_x. \quad (25)$$

where  $\mu_x$  is the mean of extended input  $X_e$ , that is originating from the integration of  $X_e$  overtime  $-\infty < t < \infty$ . Note that  $\mu_x$  in (25) is recursively updated and also adapts to changing learning environments. The use of a mixture of Gaussians can be implemented to address the dependence on the normal distribution but costs high computational complexity and not suitable for real-time implementation.

By referring to equation (22), the variance is obtained from  $\vartheta_x = E[x_p^2] - E[x_p]^2$ , where the second term is simply  $E[x_p]^2 = E[x_p] \times E[x_p]$  and the first term can be formulated as  $E[x_p^2] = W_i (\mu_x)^2$ . Combining these results, the

final expression for  $N_s$  formula is obtained. Since  $N_s$  depends on both bias and variance, a high value of  $N_s$  indicate that either the high bias (over-simplified network with measly rules) or the high variance (over-complex network with numerous rules). To maintain the network capacity with respect to the complexity, the concept of bias-variance trade-off is applied to this structural evolution mechanism. The network structure is having a low approximation capacity, if the  $\beta_x$  value is high. Therefore, the number of rules has to increase. On the contrary, a high value of  $\vartheta_x$  is due to the excess number of rules. In this case, the number of rules has to reduce. Both of these mechanisms are applied to adapt the network elastically in order to reach the optimum approximation capacity. Two criteria for rule growing and pruning are formulated respectively as follows:

(i) *Rule growing*: The criteria for rule growing is denoted by:

$$\mu_\beta(t) + \sigma_\beta(t) \geq \mu_\beta^{min} + \Gamma\sigma_\beta^{min}, \quad (26)$$

where  $\mu_\beta(t)$  is the mean of bias and  $\sigma_\beta(t)$  is the standard deviation of the system output at a time  $t$ . In the right side, the notation  $\mu_\beta^{min}$  is the minimum value of the mean bias and the  $\sigma_\beta^{min}$  is the minimum standard deviation of bias which have ever existed. This minimum value is reset each time the growing condition is satisfied.

(ii) *Rule pruning*: The similar notations is used to express the rule pruning condition as shown below

$$\mu_\vartheta(t) + \sigma_\vartheta(t) \geq \mu_\vartheta^{min} + \zeta\sigma_\vartheta^{min}. \quad (27)$$

The minimum value of the mean and standard deviation of variance is reset whenever rule pruning is executed. The growing and pruning parameter is designed to be adaptable as  $\Gamma = 1.5 \exp(-\beta_e^2) + 0.5$  and  $\zeta = 1.5 \exp(-\vartheta_x) + 0.5$ . These parameters are varying between 0.5 and 2 and behaving as the confidence interval ranges from  $0.5\sigma$  ( $\approx 38\%$ ) to  $2\sigma$  ( $\approx 95\%$ ). If the network bias or variance is high the confidence level is low, conversely if these are low, the confidence level is higher. That is, a new rule is added in the case of high bias whereas an inactive rule is removed in the case of high variance.

The rule pruning condition is based on rule significance parameter ( $RS_i$ ) formulated from the absolute value of the network output expectation in (25). The  $RS_i$  for  $i$ -th rule is calculated as follows:

$$RS_i = \|W_i \mu_x\|_1. \quad (28)$$

The rule of interest is that having the lowest statistical contribution (28). Hence, the  $j$ -th rule is pruned if the condition in (29) is satisfied

$$\arg \min_{i \in [1, 2, 3, \dots, r(t)]} (RS_i) = RS_j. \quad (29)$$

This elastic learning feature is capable of tracking any variations of plant dynamic without redesigning from scratch - common practise for a fixed and offline controller. In other words, it copes with different flight missions autonomously without applying pre-fixed controller gains.

### 3.2 Adaptation of network parameters

The hyper-plane parameters corresponding to the winning rule is only updated at each sampling instant. The winning rule is evaluated with the same network significance as outlined in (28). The  $i$ -th rule is the winning rule if the condition below is satisfied

$$\arg \max_{k \in [1, 2, 3, \dots, r(t)]} (RS_k) = RS_i. \quad (30)$$

The adaptation of the winning rule parameters at a time instant  $t$  ( $W_i(t)$ ) is designed to bring the tracking error to the sliding surface. Therefore, the cost function is chosen from the sliding surface function and it is assumed as  $v_{us}(t) \approx s_s(t)$ . By recalling equations (14), (17), and (18), the cost function is described below

$$\begin{aligned} J(t) &= \int_0^t s_s(\tau)^2 d\tau, \\ &= \int_0^t (v_{ux}(\tau) + v_{up}(\tau))^2 d\tau, \\ &= \int_0^t (v_{ux}(\tau) + W_i(\tau)\Lambda_i(\tau))^2 d\tau. \end{aligned} \quad (31)$$

The condition for optimality can be stated as  $\frac{\partial J(t)}{\partial W_i(t)} = 0$ . The adaptation rule given in (32) is obtained by following the derivation given in [52]

$$\begin{aligned} \frac{\partial J(t)}{\partial W_i(t)} &= 0, \\ 0 &= \int_0^t \Lambda_i(\tau) v_{ux}(\tau) d\tau + \int_0^t \Lambda_i(\tau) \Lambda_i(\tau)^T d\tau W_i(t), \\ W_i(t) &= - \left[ \int_0^t \Lambda_i(\tau) \Lambda_i(\tau)^T d\tau \right]^{-1} \int_0^t \Lambda_i(\tau) v_{ux}(\tau) d\tau. \end{aligned} \quad (32)$$

Let  $P_i(t) = \left[ \int_0^t \Lambda_i(\tau) \Lambda_i(\tau)^T d\tau \right]^{-1}$ , then (32) can be re-written as:

$$W_i(t) = -P(t) \int_0^t \Lambda_i(\tau) v_{ux}(\tau) d\tau. \quad (33)$$

By taking the derivative of above equation and simplifying the mathematical expression gives the following formula for weight update

$$\dot{W}_i(t) = -P_i(t) \Lambda_i(t) s_s(t), \quad \text{where } W(0) = W_0 \in \mathbb{R}^{R \times n}. \quad (34)$$

The matrix  $P_i(t)$  is updated recursively without recording all data samples as given below

$$\dot{P}_i(t) = -P_i(t) \Lambda_i(t) \Lambda_i^T(t) P_i(t), \quad (35)$$

where  $P_i(0) = P_{i_0} > 0 \in \mathbb{R}^{n \times n}$ . The pseudocode of PAC controller is presented in Algorithm 1.

## 4 Experimental Results

To evaluate the tracking and disturbance rejection properties of the PAC, several experiments are conducted using a quadrotor UAV<sup>1</sup>. The details of the experimental hardware used and the results of trajectory tracking, disturbance rejection are explained in the following two subsections.

### 4.1 Experimental Setup and Methodology

The experiments are conducted in an indoor environment using a quadrotor UAV of dimension 25 cm between the rotors with a propeller of diameter 9 inches. The UAV has onboard Pixhawk autopilot hardware interfaced to a Raspberry-Pi3 computer. The position and orientation of the UAV are precisely measured using OptiTrack vision system having eight infrared cameras. The position and orientation data are transmitted over a wifi network to a Ground Control Station (GCS) computer at a rate of 240 Hz. The control algorithm is executed in MATLAB environment inside the GCS and the control input is transmitted to the Raspberry-Pi3 computer via wifi network. The Raspberry-Pi3 computer publishes the reference velocity inputs to the Pixhawk via Robot Operating System (ROS) platform. For the inner loop velocity tracking control, a PID controller is used. The architecture of the controller implementation is shown in Fig. 4. Our experimental setup is depicted in Fig. 5.

### 4.2 Results and Analysis

The performance of PAC is experimentally evaluated for tracking various challenging trajectories as well as interaction scenarios. The typical trajectories considered here are circular and eight shaped as they actuate the baseline system dynamics more when compared to a straight line or rectangular trajectories. Moreover, when UAV is navigating in a restricted environment having obstacles, the admissible trajectories will be of circular or eight shaped in nature. For the interaction case, close proximity effects are tested including ground and ceiling effects. The experiments are conducted without any disturbance input and also for the case of wind disturbances generated using a fan. All these cases are illustrated in Fig. 6. The proposed controller PAC is compared against the baseline SMC to demonstrate the advantage of online adaptation law as well as an elastic network structure. In the presence of wind disturbances, ground and ceiling effects, the evaluations are quantified using Root Mean Square Error (RMSE) values, which is defined as given below

$$RMSE = \sqrt{\frac{1}{N} \sum_{k=1}^N \bar{e}(k)^T \bar{e}(k)}, \quad (36)$$

**Algorithm 1** Parsimonious Autonomous Controller (PAC)

---

```

1: function PAC( $x_r, x, t$ )
2:   if  $t = 0$  then
3:     Initialize:  $W(0), P(0), r(0)$ 
4:   else
5:     Compute:  $e, \int e$ 
6:     Get:  $X_e = [1; e; \int e; x]$ 
7:     —Feedforward step:—
8:     for  $i = 1$  to  $R$  do
9:       Compute:  $\delta[i], \mu[i]$ 
10:      Compute:  $\lambda[i], \Lambda[i], O[i]$ 
11:    end for
12:     $v_{up} = \text{sum}(O[i])$ 
13:    —Calculate control signal—
14:    Compute:  $s_s$ 
15:     $v_{us} = \text{sat}(s_s, a_m)$ 
16:     $v_{ux} = v_{us} - v_{up}$ 
17:    —Rule significance—
18:    Compute:  $\mu_x = \text{recursiveMean}(X_e)$ 
19:     $RS = \text{abs}(W\mu_x)$ 
20:    —Mean bias and variance calculation—
21:    Compute:  $\beta_x^2(t), \mu_\beta(t), \sigma_\beta(t)$ 
22:    Compute:  $\vartheta_x(t), \mu_\vartheta(t), \sigma_\vartheta(t)$ 
23:    —Rule growing mechanism—
24:    if  $\mu_\beta(t) + \sigma_\beta(t) \geq \mu_\beta^{min} + \Gamma\sigma_\beta^{min}$  then
25:      Grow:  $r(t) = r(t) + 1$ 
26:       $W[r(t)] = W_{i0}$ 
27:       $P[r(t)] = P_{i0}$ 
28:       $\mu_\beta^{min} = \mu_\beta(t)$ 
29:       $\sigma_\beta^{min} = \sigma_\beta(t)$ 
30:    end if
31:    —Rule pruning mechanism—
32:    if  $r(t) > 1$  then
33:      if  $\mu_\vartheta(t) + \sigma_\vartheta(t) \geq \mu_\vartheta^{min} + \zeta\sigma_\vartheta^{min}$  then
34:        Prune:  $r(t) = r(t) - 1$ 
35:        if  $\min(RS) = RS_j$  then
36:           $W[j] = []$ 
37:           $P[j] = []$ 
38:        end if
39:         $\mu_\beta^{min} = \mu_\beta(t)$ 
40:         $\sigma_\beta^{min} = \sigma_\beta(t)$ 
41:      end if
42:    end if
43:    —Winning rule parameters update—
44:    if  $\max(RS) = RS_i$  then
45:       $\dot{P}[i] = -P[i]\lambda[i]\lambda[i]^T P[i]$ 
46:       $P[i] = P[i] + \dot{P}[i] dt$ 
47:       $\dot{W}[i] = -P[i]\lambda[i]s_s$ 
48:       $W[i] = W[i] + \dot{W}[i] dt$ 
49:    end if
50:  end if
51:  output  $v_{ux}$ 
52: end function

```

---

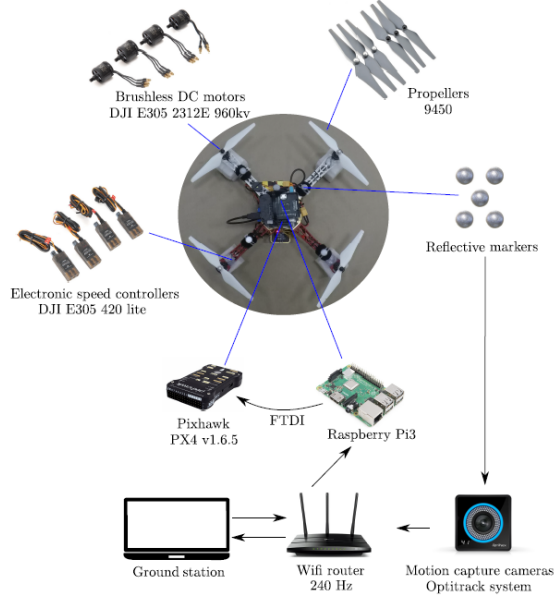


Figure 5: Experimental setup: Quadrotor and its components

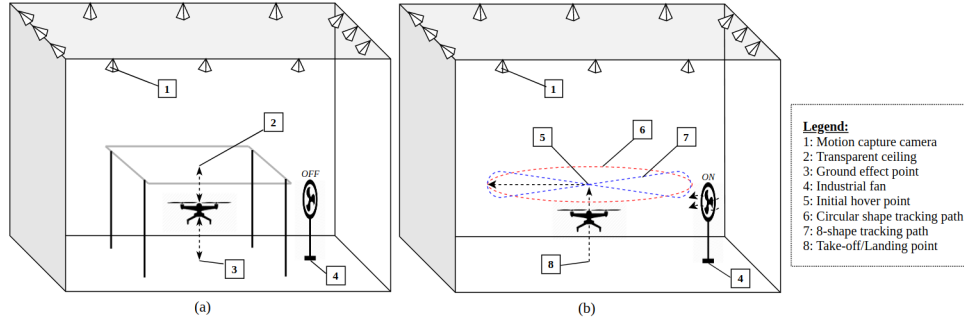


Figure 6: Experimental setup in motion capture laboratory: (a) Setup to be used for the experiment in CASE C including the transparent ceiling on top of the UAV and ground-effect; (b) Setup for circular, 8-shape tracking CASE A (without disturbance) and B to test the UAV with wind gust disturbance blown by an industrial fan

where  $\bar{e}(k) = [e_x(k), e_y(k), e_z(k)]^T$  and  $N = \frac{T_f}{t_s}$ , with  $T_f$  is the total time,  $t_s = 0.01$  s is the sampling interval and  $k$  is the sampling instant. The SMC parameters for comparison are given in Table 1.

Another important situation arises when the UAV operates in close proximity to the ceiling or the ground. The interactions between the propeller wake and the ceiling or ground act as input disturbance to the system. Experiments are conducted for the case of tracking a square wave with upper and lower limits set close to ceiling and ground, respectively. Each of the above-mentioned experimental cases is explained below in detail.

<sup>1</sup>Experimental video is available in: <https://youtu.be/-nGhMzvB7oE>

Table 1: SMC parameters used for experiments

Control	SMC parameters
<b><i>x</i>-position</b>	$k_1=1.0, k_2=0.001, k_3=0.0, a_m=0.8$
<b><i>y</i>-position</b>	$k_1=1.0, k_2=0.001, k_3=0.0, a_m=0.8$
<b>Altitude <i>z</i></b>	$k_1=0.35, k_2=0.01, k_3=0.65, a_m=0.8$

*CASE A: Circular and eight shaped trajectory tracking.*

A circle of diameter 3 m is taken as the reference trajectory. The equation for the reference trajectory is given below:

$$x_r(t) = x_c + A_r \cos\left(\frac{2\pi t}{T_c}\right), \quad (37)$$

$$y_r(t) = y_c + A_r \sin\left(\frac{2\pi t}{T_c}\right), \quad (38)$$

where  $(x_c, y_c)$  is the centre of the circle,  $A_r$  is the radius in m and  $T_c$  is the time period in s. Here  $(x_c, y_c) = (0, 0)$ ,  $A_r = 1.5$  m and  $T_c = 10$  s. The trajectory followed by the UAV and the reference circular trajectory is shown in Fig. 7. The UAV follows a straight line initially to intercept the circle at  $(1.5, 0)$ . The velocity command generated by PAC and the velocity of UAV is shown in Fig. 8. A constant non-zero velocity reference is generated by PAC initially to follow a straight line to intercept the circle. A sinusoidal velocity command is generated by PAC within the saturation velocity of 1 m/s along any axis. The evolution of rules with respect to time for the generation of reference  $v_x$  and  $v_y$  using PAC is shown in Fig. 9. The number of rules  $(r_x(t), r_y(t))$  is very small for time  $t \leq 10$  s as a straight line is followed. The number of rules  $(r_x(t), r_y(t))$  increases during the initial transition from the straight line to the circular trajectory. As the UAV continues to track the circular trajectory, the number of rules  $(r_x(t), r_y(t))$  decreases for  $t \geq 20$  s. The neuro-fuzzy network adapts to the circular trajectory and as a result of that, the excess number of rules are pruned for  $t \geq 20$  s. The number of rules generated is maximum during the transition from the straight line to the circular trajectory, ie. for  $10 < t < 20$  s. The eight shaped reference trajectory is generated by

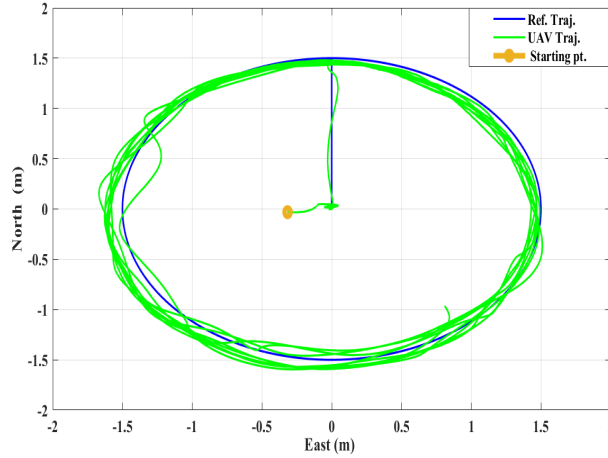


Figure 7: Circle shaped trajectory tracking using PAC

$$x_r(t) = x_c + A_x \sin\left(\frac{2\pi t}{T_x}\right), \quad (39)$$

$$y_r(t) = y_c + A_y \sin\left(\frac{2\pi t}{T_y}\right), \quad (40)$$

where the time periods  $T_x = 20$  s and  $T_y = 10$  s respectively. The amplitudes of the sinusoidal signals are  $A_x = 1.5$  m and  $A_y = 0.75$  m respectively. The centre coordinates are  $(x_c, y_c) = (0, 0)$ . The reference trajectory and the response of the UAV attained with PAC are shown in Fig. 10. The corresponding velocity command profile and UAV velocity profile are shown in Fig. 11. The PAC generates a higher frequency velocity command along Y-axis when compared to X-axis in concurrence with (39) and (40). The rule evolution for eight shaped trajectory tracking is shown in Fig. 12. The number of rules  $r_y(t)$  is smaller when compared to  $r_x(t)$  as the amplitude and the time period of the sinusoidal velocity along Y-axis is lower when compared to that of X-axis. The difference in amplitude and time period makes the UAV to travel higher distance along X-axis when compared to that along Y-axis as seen from Fig. 10.

*CASE B: Trajectory tracking under wind disturbances.*

The effect of output disturbance on the performance of PAC is verified by generating a wind disturbance using a fan. A comparison is provided with SMC for tracking circular and eight shaped trajectories mentioned in CASE A. The trajectories obtained using PAC and SMC are shown in Fig. 13 for the case of tracking the circular trajectory. The

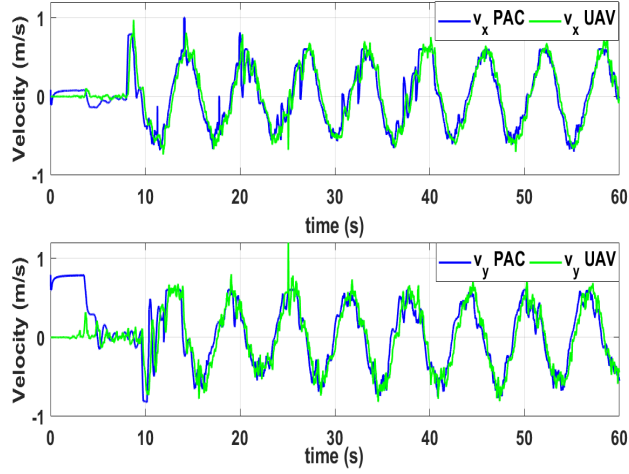


Figure 8: Velocity command generated by PAC and UAV velocity for circle shaped trajectory tracking

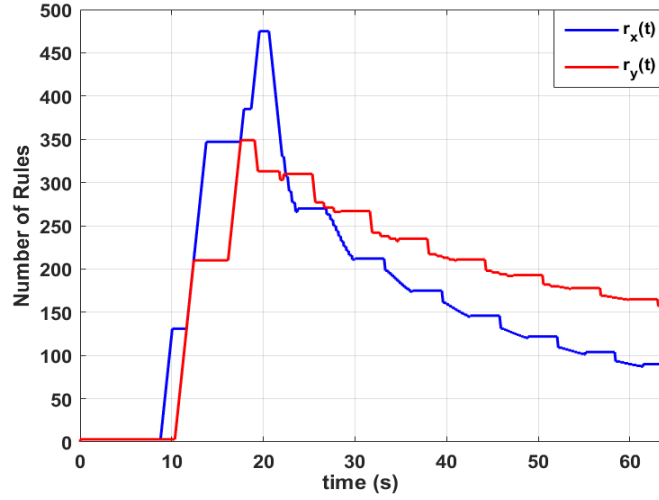


Figure 9: Rule evolution for circle shaped trajectory tracking

direction of the wind is shown by the arrow. It can be observed that with PAC, the deviation from the trajectory is less when compared to that of using SMC. For the case of tracking eight shaped trajectories with wind disturbance, the responses of PAC and SMC are shown in Fig. 14. The RMSE values shown in Table 2 indicate that PAC excel SMC in rejecting wind disturbances.

Table 2: Summary of RMSE values of the experiments

UAV Mission	RMSE no wind (m)		RMSE with wind (m)	
	SMC	PAC	SMC	PAC
Circular-shape	0.2349	0.1515	0.2602	0.1768
8-shape	0.1255	0.1216	0.1945	0.1254
Altitude with interaction	0.0987	0.0859	N/A	N/A

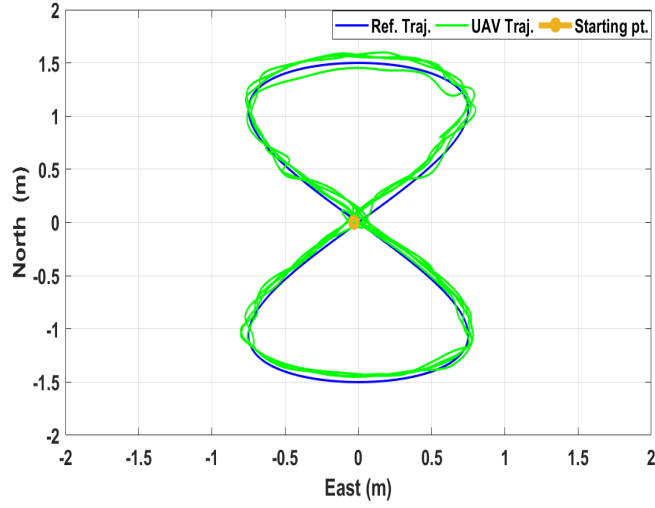


Figure 10: Eight shaped trajectory tracking using PAC

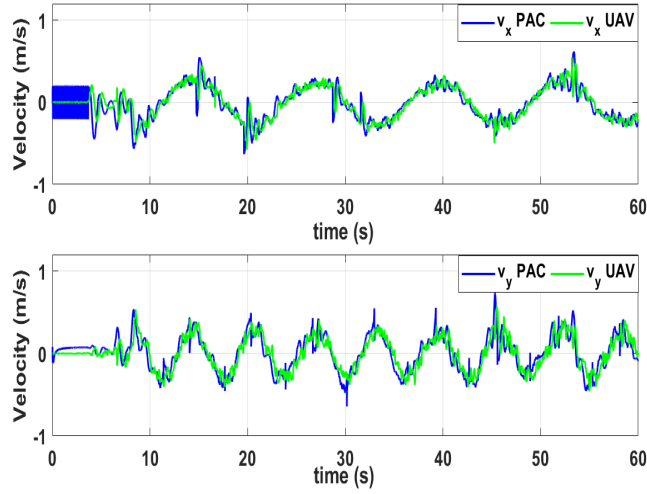


Figure 11: Velocity command generated by PAC and UAV velocity for eight shaped trajectory tracking

*CASE C: Altitude tracking in the presence of ceiling and ground interaction effects.*

The interaction between the propeller wake and ceiling/ground generates additional forces that can be treated as input disturbance acting on the system. A square wave of amplitude 0.6 m and time period 21 s is given as reference trajectory for altitude tracking. The responses of PAC and SMC are given in Fig. 15. The reference altitude varies from 0.25 - 0.85 m. As observed from Fig. 15, the input disturbance due to the ceiling effect is more prominent when compared to the disturbance created by the ground effect. The SMC control has a peak overshoot of 10.5 % while tracking 0.85 m altitude reference, whereas PAC has only 1.8 % peak overshoot. In the presence ground effect, it is hard to remain closer to the reference altitude due to the additional upward force generated by the rotors. For a reference altitude of 0.25 m, the altitude envelope of PAC is in between 0.241-0.301 m when compared to 0.213-0.332 m achieved by SMC. The RMSE values are given in Table 2 with PAC having the lowest value. Thus PAC is more effective than SMC in attenuating input disturbances.

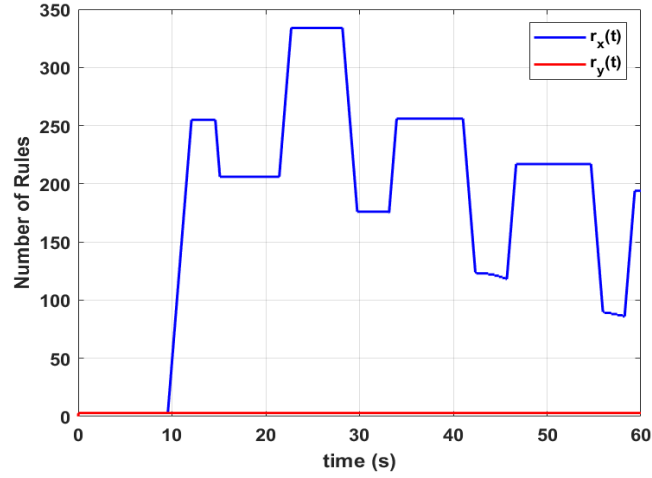


Figure 12: Rule evolution for eight shaped trajectory tracking

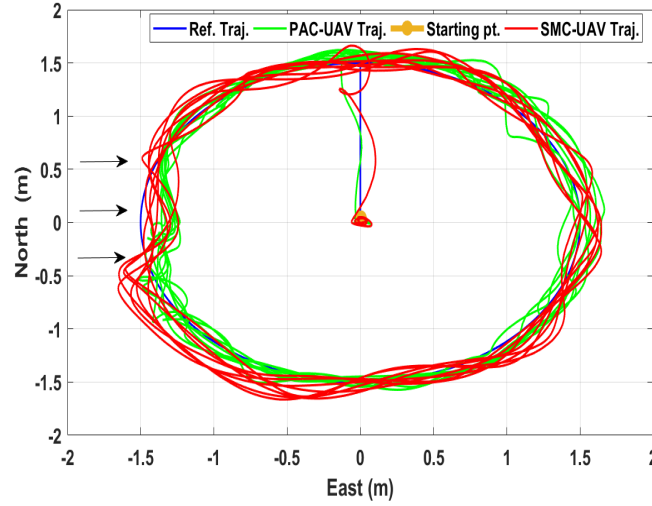


Figure 13: Comparison between PAC and SMC for circle shaped trajectory tracking with wind disturbance (wind direction is shown by the arrow)

## 5 Conclusion

This paper presents an autonomous controller consisting of an evolving neuro-fuzzy structure and SMC. After defining the mathematical model, the challenges are identified for the problem arises during the interaction phase as well as tracking while flying through the wind gust disturbance case. Afterward, proposed evolving neuro-fuzzy structure and SMC are introduced. The experiments showed that the system performance under several different missions is recovered when the autonomous controller is applied. This controller eases the design and implementation process as it does not require any further tuning for a different task, a precise system model, and exact information about the environment. For the sake of reproducible research, the link to our experimental video is also provided.

An interesting extension of this work would be the application to more challenging scenarios such as trajectory and target tracking in an outdoor environment [53]. In this context, reinforcement learning-based approaches (e.g., [54],[55]) can be explored within interaction scenarios for the field tests.

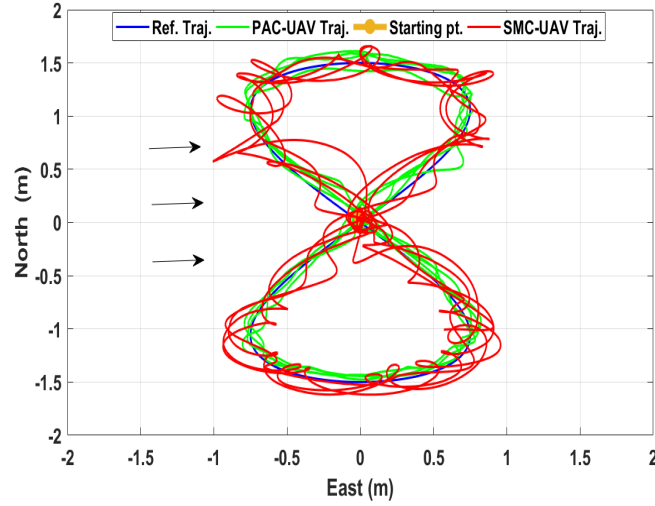


Figure 14: Comparison between PAC and SMC for eight shaped trajectory tracking with wind disturbance (wind direction is shown by the arrow)

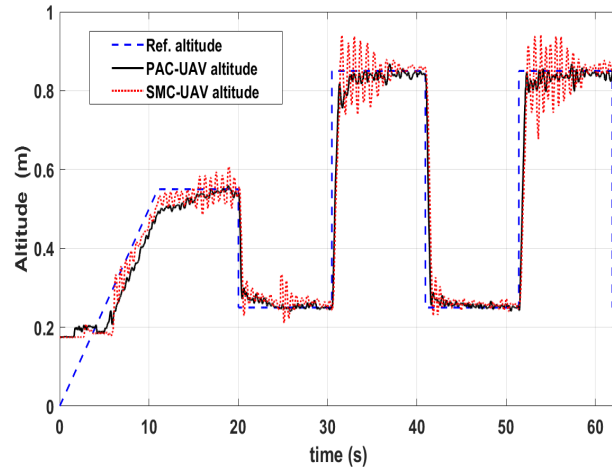


Figure 15: Comparison between PAC and SMC for altitude tracking in the presence of ceiling and ground effects

## Acknowledgment

The authors would like to thank the financial support provided by NTU internal grant for the project on Large Vertical Take-Off and Landing (VTOL) Research Platform: Prototype development and demonstration (NTU internal funding).

## 6 References

1. A. C. Woods and H. M. La, "A novel potential field controller for use on aerial robots," *IEEE Transactions on Systems, Man, and Cybernetics: Systems*, vol. 49, no. 4, pp. 665-676, 2017.
2. S. Islam, P. X. Liu, A. El Saddik, R. Ashour, J. Dias, and L. D. Seneviratne, "Artificial and virtual impedance interaction force reflection-based bilateral shared control for miniature unmanned aerial vehicle," *IEEE Transactions on Industrial Electronics*, vol. 66, no. 1, pp. 329-337, 2019.
3. K. Dorling, J. Heinrichs, G. G. Messier, and S. Magierowski, "Vehicle routing problems for drone delivery," *IEEE Transactions on Systems, Man, and Cybernetics: Systems*, vol. 47, no. 1, pp. 70-85, 2016.
4. S. Saripalli, J. F. Montgomery, and G. S. Sukhatme, "Vision-based autonomous landing of an unmanned aerial vehicle," in *Robotics and automation, 2002. Proceedings. ICRA 02. IEEE international conference on*, vol. 3. IEEE,

2002, pp. 2799-2804.

5. F. Huber, K. Kondak, K. Krieger, D. Sommer, M. Schwarzbach, M. Laiacker, I. Kossyk, S. Parusel, S. Haddadin, and A. Albu-Schaffer, "First analysis and experiments in aerial manipulation using fully actuated redundant robot arm," in *Intelligent Robots and Systems (IROS)*, 2013 IEEE/RSJ International Conference on. IEEE, 2013, pp. 3452-3457.
6. Z. Yu, K. Nonami, J. Shin, and D. Celestino, "3d vision based landing control of a small scale autonomous helicopter," *International Journal of Advanced Robotic Systems*, vol. 4, no. 1, p. 7, 2007.
7. P. Pounds, R. Mahony, and P. Corke, "Modelling and control of a large quadrotor robot," *Control Engineering Practice*, vol. 18, no. 7, pp. 691-699, 2010.
8. P. E. Pounds, D. R. Bersak, and A. M. Dollar, "Grasping from the air: Hovering capture and load stability," in *Robotics and Automation (ICRA)*, 2011 IEEE International Conference on. IEEE, 2011, pp. 2491-2498.
9. D. B. P.E.I. Pounds and A. Dollar, "Stability of small-scale uav helicopters and quadrotors with added payload mass under pid control," *Autonomous Robots*, vol. 33, no. 1-2, pp. 129-142, 2012.
10. K. Nonaka and H. Sugizaki, "Integral sliding mode altitude control for a small model helicopter with ground effect compensation," in *American Control Conference (ACC)*, 2011. IEEE, 2011, pp. 202-207.
11. D. Lee, T. Ryan, and H. J. Kim, "Autonomous landing of a vtol uav on a moving platform using image-based visual servoing," in *Robotics and Automation (ICRA)*, 2012 IEEE International Conference on. IEEE, 2012, pp. 971-976.
12. T. K. Roy, M. Garratt, H. Pota, and M. Samal, "Robust altitude control for a small helicopter by considering the ground effect compensation," in *Intelligent Control and Automation (WCICA)*, 2012 10th World Congress on. IEEE, 2012, pp. 1796-1800.
13. T. K. Roy and A. Suman, "Adaptive backstepping controller for altitude control of a small scale helicopter by considering the ground effect compensation," in *Informatics, Electronics and Vision (ICIEV)*, 2013 International Conference on. IEEE, 2013, pp. 1-5.
14. T. K. Roy, "Robust adaptive backstepping controller for altitude control of a small scale helicopter by considering the ground effect compensation," *Universal Journal of Control and Automation*, vol. 1, no. 2, pp. 52-57, 2013.
15. X. He, M. Calaf, and K. K. Leang, "Modeling and adaptive nonlinear disturbance observer for closed-loop control of in-ground-effects on multi-rotor uavs," in *ASME 2017 Dynamic Systems and Control Conference*. American Society of Mechanical Engineers, 2017, pp. V003T39A004-V003T39A004.
16. B. Herisse, T. Hamel, R. Mahony, and F.-X. Russotto, "Landing a vtol unmanned aerial vehicle on a moving platform using optical flow," *IEEE Transactions on robotics*, vol. 28, no. 1, pp. 77-89, 2012.
17. L. Danjun, Z. Yan, S. Zongying, and L. Geng, "Autonomous landing of quadrotor based on ground effect modelling," in *Control Conference (CCC)*, 2015 34th Chinese. IEEE, 2015, pp. 5647-5652.
18. H. Nobahari and A. Sharifi, "Continuous ant colony filter applied to online estimation and compensation of ground effect in automatic landing of quadrotor," *Engineering Applications of Artificial Intelligence*, vol. 32, pp. 100-111, 2014.
19. C. Hooi, F. Lagor, and D. Paley, "Flow sensing for height estimation and control of a rotor in ground effect: Modeling and experimental results," in *71th Annual Forum of the American Helicopter Society*, 2015.
20. H. Nobahari and H. Mohammadkarimi, "Application of model aided inertial navigation for precise altimetry of unmanned aerial vehicles in ground proximity," *Aerospace Science and Technology*, vol. 69, pp. 650-658, 2017.
21. D. Yeo, N. Sydney, D. A. Paley, and D. Sofge, "Onboard flow sensing for downwash detection and avoidance with a small quadrotor helicopter," in *AIAA Guidance, Navigation, and Control Conference*, 2015, p. 1769.
22. D. W. Yeo, N. Sydney, D. A. Paley, and D. Sofge, "Downwash detection and avoidance with small quadrotor helicopters," *Journal of Guidance, Control, and Dynamics*, vol. 40, no. 3, pp. 692-701, 2016.
23. P. Sanchez-Cuevas, G. Heredia, and A. Ollero, "Multicopter uas for bridge inspection by contact using the ceiling effect," in *Unmanned Aircraft Systems (ICUAS)*, 2017 International Conference on. IEEE, 2017, pp. 767-774.
24. Q. Delamare, P. R. Giordano, and A. Franchi, "Toward aerial physical locomotion: The contact-fly-contact problem," *IEEE Robotics and Automation Letters*, vol. 3, no. 3, pp. 1514-1521, 2018.
25. C. Powers, D. Mellinger, A. Kushleyev, B. Kothmann, and V. Kumar, "Influence of aerodynamics and proximity effects in quadrotor flight," in *Experimental robotics*. Springer, 2013, pp. 289-302.
26. B. B. Kocer, T. Tjahjowidodo, and G. G. L. Seet, "Centralized predictive ceiling interaction control of quadrotor vtol uav," *Aerospace Science and Technology*, vol. 76, pp. 455-465, 2018.
27. T. Gao, S. Yin, J. Qiu, H. Gao, and O. Kaynak, "A partial least squares aided intelligent model predictive control approach," *IEEE Transactions on Systems, Man, and Cybernetics: Systems*, vol. 48, no. 11, pp. 2013-2021, 2017.
28. K. Alexis, G. Nikolakopoulos, and A. Tzes, "Switching model predictive attitude control for a quadrotor helicopter subject to atmospheric disturbances," *Control Engineering Practice*, vol. 19, no. 10, pp. 1195-1207, 2011.
29. B. B. Kocer, T. Tjahjowidodo, and G. G. L. Seet, "Model predictive uav-tool interaction control enhanced by external forces," *Mechatronics*, vol. 58, pp. 47-57, 2019.
30. A. Das, K. Subbarao, and F. Lewis, "Dynamic inversion with zerodynamics stabilisation for quadrotor control," *IET control theory and applications*, vol. 3, no. 3, pp. 303-314, 2009.
31. E. J. Smeur, G. C. de Croon, and Q. Chu, "Cascaded incremental nonlinear dynamic inversion for mav disturbance

- rejection," *Control Engineering Practice*, vol. 73, pp. 79-90, 2018.
32. Z. T. Dydek, A. M. Annaswamy, and E. Lavretsky, "Adaptive control of quadrotor uavs: A design trade study with flight evaluations," *IEEE Transactions on control systems technology*, vol. 21, no. 4, pp. 1400-1406, 2013.
33. Y. Zou and Z. Meng, "Immersion and invariance-based adaptive controller for quadrotor systems," *IEEE Transactions on Systems, Man, and Cybernetics: Systems*, 2018.
34. S. Islam and X. P. Liu, "Robust sliding mode control for robot manipulators," *IEEE Transactions on Industrial Electronics*, vol. 58, no. 6, pp.2444-2453, 2011.
35. N. Wang, S. Su, M. Han, and W. Chen, "Backpropagating constraints based trajectory tracking control of a quadrotor with constrained actuator dynamics and complex unknowns," *IEEE Transactions on Systems, Man, and Cybernetics: Systems*, vol. 49, no. 7, pp. 1322-1337, July 2019.
36. L. Besnard, Y. B. Shtessel, and B. Landrum, "Quadrotor vehicle control via sliding mode controller driven by sliding mode disturbance observer," *Journal of the Franklin Institute*, vol. 349, no. 2, pp. 658-684, 2012.
37. B. Tian, J. Cui, H. Lu, Z. Zuo, and Q. Zong, "Adaptive finite-time attitude tracking of quadrotors with experiments and comparisons," *IEEE Transactions on Industrial Electronics*, 2019.
38. H. Rois, R. Falcon, O. A. Gonzalez, and A. Dzul, "Continuous slidingmode control strategies for quadrotor robust tracking: real-time application," *IEEE Transactions on Industrial Electronics*, vol. 66, no. 2, pp.1264-1272, 2019.
39. L. Doitsidis, K. P. Valavanis, N. C. Tsourveloudis, and M. Kontitsis, "A framework for fuzzy logic based uav navigation and control," in *IEEE International Conference on Robotics and Automation, 2004. Proceedings. ICRA 04. 2004*, vol. 4. IEEE, 2004, pp. 4041-4046.
40. V. Artale, M. Collotta, G. Pau, and A. Ricciardello, "Hexacopter trajectory control using a neural network," in *AIP Conference Proceedings*, vol. 1558, no. 1. AIP, 2013, pp. 1216-1219.
41. B. Xu, "Composite learning finite-time control with application to quadrotors," *IEEE Transactions on Systems, Man, and Cybernetics: Systems*, vol. 48, no. 10, pp. 1806-1815, Oct 2018.
42. S. Kurnaz, O. Cetin, and O. Kaynak, "Adaptive neuro-fuzzy inference system based autonomous flight control of unmanned air vehicles," *Expert Systems with Applications*, vol. 37, no. 2, pp. 1229-1234, 2010.
43. F. Santoso, M. A. Garratt, and S. G. Anavatti, "Hybrid pd-fuzzy and pd controllers for trajectory tracking of a quadrotor unmanned aerial vehicle: Autopilot designs and real-time flight tests," *IEEE Transactions on Systems, Man, and Cybernetics: Systems*, 2019.
44. F. Santoso, M. A. Garratt, S. G. Anavatti, and I. Petersen, "Robust hybrid nonlinear control systems for the dynamics of a quadcopter drone," *IEEE Transactions on Systems, Man, and Cybernetics: Systems*, 2018.
45. M. M. Ferdous, M. Pratama, S. G. Anavatti, M. A. Garratt, and Y. Pan, "Generic evolving self-organizing neuro-fuzzy control of bio-inspired unmanned aerial vehicles," *IEEE Transactions on Fuzzy Systems*, 2019.
46. M. M. Ferdous, M. Pratama, S. G. Anavatti, M. A. Garratt, and E. Lughofer, "Pac: A novel self-adaptive neuro-fuzzy controller for micro aerial vehicles," *arXiv preprint arXiv:1811.03764*, 2018.
47. K. Harikumar, J. Senthilnath, and S. Sundaram, "Mission aware motion planning (map) framework with physical and geographical constraints for a swarm of mobile stations," *IEEE Transactions on Cybernetics*, 2019.
48. M. Chen, S. Xiong, and Q. Wu, "Tracking flight control of quadrotor based on disturbance observer," *IEEE Transactions on Systems, Man, and Cybernetics: Systems*, 2019.
49. N. Wang, S.-F. Su, M. Han, and W.-H. Chen, "Backpropagating constraints-based trajectory tracking control of a quadrotor with constrained actuator dynamics and complex unknowns," *IEEE Transactions on Systems, Man, and Cybernetics: Systems*, vol. 49, no. 7, pp. 1322-1337, 2018.
50. J. Xu, P. Shi, C.-C. Lim, C. Cai, and Y. Zou, "Reliable tracking control for under-actuated quadrotors with wind disturbances," *IEEE Transactions on systems, man, and cybernetics: systems*, 2018.
51. M. M. Ferdous, M. Pratama, S. G. Anavatti, and M. A. Garratt, "Palm: An incremental construction of hyperplanes for data stream regression," *IEEE Transactions on Fuzzy Systems*, 2019.
52. J. A. Farel and M. M. Polycarpou, *Adaptive Approximation Based Control*. Wiley-Interscience, 2006.
53. Y. Liu, Q. Wang, H. Hu, and Y. He, "A novel real-time moving target tracking and path planning system for a quadrotor uav in unknown unstructured outdoor scenes," *IEEE Transactions on Systems, Man, and Cybernetics: Systems*, 2018.
54. H. Wu, S. Song, K. You, and C. Wu, "Depth control of model-free auvs via reinforcement learning," *IEEE Transactions on Systems, Man, and Cybernetics: Systems*, 2018.
55. Y. Wang, J. Sun, H. He, and C. Sun, "Deterministic policy gradient with integral compensator for robust quadrotor control," *IEEE Transactions on Systems, Man, and Cybernetics: Systems*, 2019.